INVESTIGATION OF THREE RECENT ATLAS V CENTAUR UPPER STAGE FRAGMENTATION EVENTS

Pavithra Ravi[(1)], Carolin Frueh[(1)], and Thomas Schildknecht[(2)]

[(1)]*Purdue University, School of Aeronautics and Astronautics, West Lafayette, IN 47907-2045, USA, Email: {ravi12, cfrueh}@purdue.edu*

[(2)]*Astronomical Institute of the University of Bern, 3012 Bern, Switzerland, Email: thomas.schildknecht@aiub.unibe.ch*

ABSTRACT

Three Centaur upper stage fragmentation events – 2009-047B, 2014-055B, 2018-079B – that took place in 2018 and 2019 are studied. Ephemerides and Two-Line Elements (TLEs) of the fragments, from three different data sources, are propagated to calculate the breakup epoch. Additionally, techniques developed by Tan and Reynolds [22] to obtain Gabbard plots, velocity & angular perturbations of the fragments, and event intensities, are applied to the Centaur upper stage events. From the results, hypotheses regarding the causes of the events are postulated. The Centaur fragmentations stray from breakup patterns exhibited by 'typical' upper stage fragmentations such as those pertaining to the historic explosive Delta upper stage events. Only one of the three events, 2018-079B, appears to have fragmented due to the combustion of leftover propellant. 2009-047B, on the other hand, likely endured a structural failure – inferred from clustered fragments and low fragment spreading speeds. A torus-shaped fragment distribution is observed for the 2014-055B event, suggesting a collision with a small piece of debris may have taken place.

Keywords: fragmentation; breakup; centaur; upper stage; space debris.

1. INTRODUCTION

The proliferation of man-made objects in orbit for scientific, defense, and commercial purposes has resulted in numerous fragmentation events. Since 1961, more than 560 in-orbit fragmentation events have taken place, most of which have been explosions of satellites and upper stages. Coupled with explosions, detonations and collisions have resulted in over 900,000 objects from 1-10 cm and over 34,000 objects larger than 10 cm crowding orbit [9]. Due to their high velocities (upwards of 7 km/s), this debris can have catastrophic impacts on operational satellites and space stations. Thus, it is pertinent to understand how such fragmentation events arise, so actions to mitigate them can be taken.

A plethora of literature pertaining to the investigation of fragmentation events exists. Earlier works from the late 1980s and 1990s primarily focused on estimating the size, mass, and dispersion of debris clouds [6] [4] [13] [14]. More recent works have been dedicated to uncovering specific breakup characteristics, such as identification of the breakup epoch and parent object [19] [8], and determining fragment velocities [11] from post-event fragment orbits. Several works have also attempted to determine the causes of various fragmentation events through the study of multiple breakup characteristics including breakup time and location, Area-to-Mass Ratio (AMR) of the fragments, fragment spreading speeds and directions, and event energy [12] [20] [10] [15] [22]. The most comprehensive of these is *Theory of Satellite Fragmentation in Orbit* by Tan and Reynolds (2020) [22], and serves as a primary reference for this paper. Additionally, ground-based experimental methods to characterize fragmentation events have taken place – these include both hyper-velocity impact studies [7] as well as pressurized-to-failure explosive propellant tank tests [16].

No thorough investigation of the Centaur upper stage fragmentation events has occurred at the time of writing. Thus, this paper aims to shed light on key breakup characteristics surrounding these events using data from multiple sources, and subsequently postulates the causes of these events.

2. CURRENT INSIGHTS

The three events were discovered based on measurements by the International Scientific Optical Network (ISON) and the Roscosmos Automated Warning System on Hazardous Situations in Outer Space (ASPOS OKP).

All three of the fragmented objects are identical Centaur upper stages launched on the Atlas V launch vehicle operated by United Launch Alliance. The Centaur upper stages are of the Single-Engine Centaur (SEC)

variant with a Pratt & Whitney RL10A-4-2 engine, using liquid oxygen and liquid hydrogen as propellant [17]. Each of the Centaur stages successfully placed US military communications satellites into Geostationary Transfer Orbits (GTO), ultimately possessing highly elliptical orbits (HEO) with relatively high perigees. The body of the Centaur is relatively large: it has a length of 12.68 m, a diameter of 3.05 m, and a dry mass of 2243 kg [1]. This is about twice the size of the Delta upper stages which famously exploded in the 1970s. Agapov and Savin found that debris resulting from the three events has increased the number of all HEO and Medium Earth Orbit (MEO) objects catalogued by 2698 – this is over 31 percent of the HEO and MEO population [2]. The breakup dates calculated by them, along with information regarding the orbits of the three parent objects are summarised in Table 1.

For ease of discussion, 2009-047B will henceforth be referred to as Event 1, 2014-055B as Event 2, and 2018-079B as Event 3.

3. DATA SOURCES

The Astronomical Institute of the University of Bern (AIUB) has long-standing scientific collaborations with ISON, the Keldysh Institute of Applied Mathematics, Moscow, and the Astronomical Scientific Center, Moscow, and observation data is regularly exchanged with them. In the context of this collaboration, the Russian colleagues timely informed AIUB about these three events and provided orbital elements for the discovered fragments. Since October 2018, AIUB has been performing observations with the ESA 1-m telescope at Tenerife, on behalf of ESA, along with its sensors – the Swiss Optical Ground Station and the Geodynamics Observatory Zimmerwald, Switzerland – these observations are to characterize debris clouds and maintain an orbit catalogue for a subset of the fragments associated with the events.

In addition to data from AIUB sensors, data from the Vimpel catalog (maintained by JSC Vimpel Interstate Corporation and Keldysh Institute of Applied Mathematics) and the Spacetrack catalog (maintained by the 18th Space Control Squadron of the US Strategic Command, USSTRATCOM) are used for this investigation. The number of fragments catalogued by each source for the three events is summarized in Table 2.

Data obtained from AIUB contained ephemerides of the fragments pertaining to February 2020. This is about 10 months after Events 1 and 3, and 1.5 years after Event 2. The fragments were catalogued in the Vimpel catalog just over a week after each of the events.
TLEs from USSTRATCOM were obtained from spacetrack.org. Only a single fragment, which inherited the parent object's international designator, has been catalogued for Event 1. Interestingly, 2009-047B's first appearance in the Spacetrack catalog is on 3rd April 2019 (10 days after the event), with no data on the pre-event parent object available. For Events 2 and 3, fragments appeared in the catalog 5 and 7 months after each event, respectively. Similar to Event 1, the first appearance of 2014-055B in the catalog was after the event, on 24th January 2019 (about 4 months after the breakup).

The methods used to compute the various breakup characteristics surrounding the three events are covered in the following sections. These were also calculated for three of the Delta upper stage fragmentation events (NOAA-3, Landsat-1, Nimbus-6), as well as the Spot-1 event. The results have been validated with those obtained in [22].

A note on terminology: 'parent' or 'pre-event parent' refers to the parent objects prior to the fragmentations. 'Parent remnant' is used to refer to the most significant fragment resulting from each event for the AIUB data. For the Vimpel data, this remnant is assumed to be the fragment with the lowest AMR value; for the Spacetrack data, the object which inherited the parent's international designator is assumed to be the parent remnant.

4. BREAKUP EPOCH

The breakup epoch is key in understanding fragmentations since it provides insight into where along the orbit the parent object was when it fragmented. Only with this information, can the spreading speeds and angular distributions of the fragments be calculated.

The breakup epoch for each of the three events is found by back-propagating the orbits of the fragments to a point in time when their mean inter-fragment distances reach a minimum value. It is pertinent that the minimum reached is a global minimum and not a local minimum – this is ensured by using an iterative sliding window scheme with increasingly smaller time steps. A Simplified General Perturbations (SGP) 4 model is used to propagate TLE data, while ephemerides are propagated using in-house numeric integration models. Perturbations due to the atmosphere, solar radiation pressure, Earth's oblateness, and third-body interactions (with the Moon and the Sun) are accounted for.

Two different distance functions, based on orbital distance and linear distance, are compared. Equation 1 shows the orbital distance function used [8].

$$D^2_{\text{orbital}} = (e_B - e_A)^2 + \left(\frac{q_B - q_A}{q_B + q_A}\right)^2 + \left(2\sin\left(\frac{I_{BA}}{2}\right)\right)^2 + \left(\frac{e_B + e_A}{2}\right)^2 \left(2\sin\left(\frac{\pi_{BA}}{2}\right)\right)^2 \quad (1)$$

Here, the subscripts 'A' and 'B' are the indices of any two fragments. e refers to the magnitude of the Laplace-Lenz vector, $\boldsymbol{e} = (\boldsymbol{v} \times \boldsymbol{c})/\mu - \boldsymbol{r}/r$. r, v, and c, refer to the magnitudes of distance, velocity, and angular momentum respectively. Emboldened variables are vectors. q is the perigee distance. I_{BA} and π_{BA} are defined in Equations 2

Table 1: Key facts surrounding the Centaur upper stage events

	Event 1 (2009-047B)	Event 2 (2014-055B)	Event 3 (2018-079B)
SSN	35816	40209	43652
Breakup date	24th Mar 2019	30th Aug 2018	6th Apr 2019
Payload	USA-207	USA-257	USA-288
Orbit (km)	34700 x 6675	35180 x 8202	35092 x 8526
Inclination (deg)	23.1	22.2	12.2

Table 2: Number of fragments catalogued by AIUB, Vimpel, and Spacetrack

	Event 1 (2009-047B)	Event 2 (2014-055B)	Event 3 (2018-079B)
AIUB	725	676	907
Vimpel	81	208	187
Spacetrack	1	69	55

and 3.

$$I_{BA} = \cos^{-1}\left(\frac{\boldsymbol{c_A} \cdot \boldsymbol{c_B}}{c_A\, c_B}\right) \tag{2}$$

$$\pi_{BA} = \omega_B - \omega_B + 2\sin^{-1}\left(S_{BA}\right) \tag{3}$$

where S_{BA} is,

$$S_{BA} = \cos\left(\frac{i_B + i_A}{2}\right)\sin\left(\frac{\Omega_B - \Omega_A}{2}\right)\sec\left(\frac{I_{BA}}{2}\right) \tag{4}$$

i refers to inclination, while Ω is the right ascension of the ascending node.
The linear distance function in Equation 5 calculates the Euclidean distance in three dimensions between two objects.

$$D_{\text{linear}} = [(r_{x,B} - r_{x,A})^2 + (r_{y,B} - r_{y,A})^2 + (r_{z,B} - r_{z,A})^2]^{\frac{1}{2}} \tag{5}$$

$r_{x,y,z}$ refer to the geocentric coordinates of the fragment in question.

For both of these functions, the following mean distances are found: inter-fragment distances (no pre-event parent), inter-fragment distances of the fragments along with the pre-event parent, and fragment distances relative to the pre-event parent. It becomes evident that using the linear distance function along with measuring fragment distances relative to the pre-event parent, consistently yields results closer to the breakup dates found by Agopov and Savin [2]. Table 3 shows the breakup times calculated for each of the three events. Entries marked with '*' correspond to the breakup date calculated in [2].

The breakup epoch calculation is sensitive to three main factors – firstly, how recent the data is to the fragmentation event (data closer to the event will require less propagation and is thus less prone to error accumulation). Secondly, if the pre-event parent data is available (the breakup algorithm performs best when the fragment distances are measured relative to the pre-event parent). Lastly, the number of fragments used. This is relevant when fragments are added to the catalog sporadically, as in the case of the Spacetrack catalog. If only a handful of fragments are added a week after the breakup, while the remaining fragments are added a few months after, using all of the data is more favorable since the benefit of having more data points outweighs the disadvantage stemming from longer propagation. Conversely, it is also possible that a large fragment data set may include outliers which could skew mean distances. This factor, along with the long propagation times for the AIUB fragments may point to the discrepancy in the breakup dates for Event 1 and Event 3 for the AIUB data.

For subsequent analysis, Vimpel breakup times are used due to their alignment with [2].

5. GABBARD DIAGRAM

A Gabbard diagram for a given event is a plot of the apogee and perigee altitudes of the fragments against their respective periods [21]. It is also customary to denote the pre-event parent on the plot.

Gabbard plots are generated for the three events for the time of breakup (corresponding to the Vimpel data). The horizontal spread of fragments on either side of the pre-event parent is indicative of the downrange velocity perturbations imparted. Fragments to the right of the parent, speed up along the orbit, while fragments to the left of the parent slow down. Similarly, the vertical spread of

Table 3: Breakup times for the three events corresponding to data sources.

	AIUB	Vimpel	Spacetrack
Event 1 (2009-047B)	12:00, 3rd Apr 2019	3:33, 24th Mar 2019*	-
Event 2 (2014-055B)	17:14, 30th Aug 2018*	22:04, 30th Aug 2018*	20:40, 30th Aug 2018*
Event 3 (2018-079B)	15:00, 7th Apr 2019	18:57, 6th Apr 2019*	16:43, 6th Apr 2019*

fragments from the apsidal lines denotes imparted radial velocity perturbations – the higher the deviation from the lines, the higher the radial velocity magnitudes.

There also exists a 'Forbidden Zone', which is between the apogee and perigee lines if the parent is ascending, and outside the lines (above the apogee line and beneath the perigee line) if the parent is descending. Fragments in this region are affected by drag.

While Gabbard diagrams for breakups in highly elliptical orbits (as for the three events) are less insightful than those for circular orbits, which possess a characteristic 'X' shape and indicate the breakup altitude, broad insights into the intensity of the event can be obtained. For instance, a more spread-out distribution would point towards fragments with relatively high velocity perturbations and specific kinetic energies.

5.1. Event 1 (2009-047B)

The Gabbard diagram for Event 1, shown in Figure 1 is rather interesting; the fragments appear to have received a relatively small impulse as can be inferred from the small range in periods and the apogee/perigee altitudes. The horizontal spread of the fragments is roughly even on both sides of the pre-event parent for the Vimpel data, but the AIUB fragments are mostly to the left of the parent. This suggests that a considerable amount of AIUB fragments slowed down in their orbits. It is interesting to note that fragments in the Vimpel catalog received minimal radial velocity perturbations, as inferred from the near-straight apsidal lines. Three outliers from the AIUB data with significantly larger periods are omitted from this Gabbard plot. The velocity perturbations of these fragments are covered in section 6.1. The parent object for Event 1 was ascending, denoting the Forbidden Zone is between the apsidal lines – this region has a clear dearth of fragments, suggesting minimal drag effects took place on the fragments.

5.2. Event 2 (2014-055B)

The Gabbard diagram for Event 2, shown in Figure 2, is more conventional than that for Event 1, spanning larger ranges of both apogee/perigee altitudes and periods. The

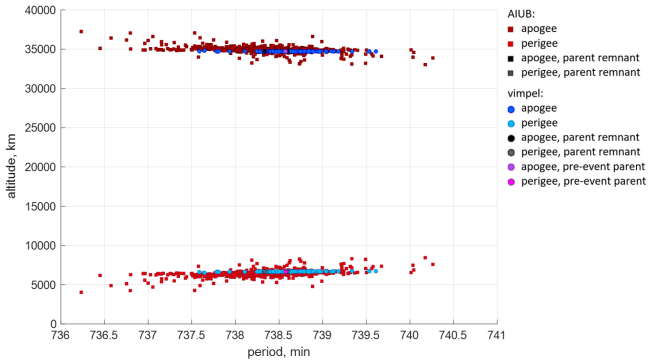

Figure 1: Event 1 (2009-047B), Gabbard diagram of fragments.

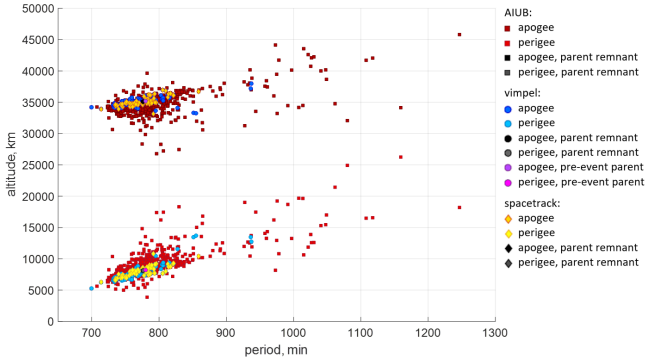

Figure 2: Event 2 (2014-055B), Gabbard diagram of fragments.

three data sources (AIUB, Vimpel, and Spacetrack) appear to be in accordance with each other. The prominent spread of AIUB fragments away from the apsidal lines suggests high radial velocities. A number of fragments (mostly AIUB and a few Vimpel) possess high periods upwards of 900 minutes – these fragments received large positive downrange impulses and thus sped up considerably along the orbit. The parent object pertaining to Event 2 was descending in its orbit – the Forbidden Zone thus lies outside of the apsidal lines. While most of the fragments lie in between the lines, the handful that are apogee the apogee line and below the perigee line are affected by drag effects.

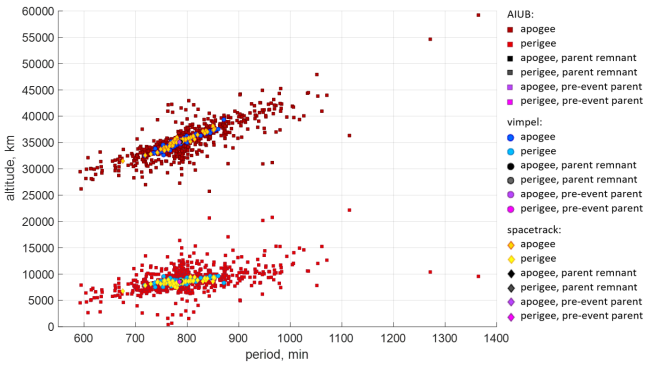

Figure 3: Event 3 (2018-079B), Gabbard diagram of fragments.

5.3. Event 3 (2018-079B)

The Gabbard diagram for Event 3 is shown in Figure 3. The Vimpel and Spacetrack data appear to be closely aligned, with the AIUB fragments extending around them, roughly symmetrically. This Gabbard plot covers the broadest ranges of periods and altitudes, suggesting this may be the highest intensity event of the three fragmentations. The largest extension of the AIUB fragments both vertically and horizontally along the two apsidal lines once again points towards high velocity perturbations encountered by these fragments. The parents for the three data lie very close together, roughly in the middle of the cluster; this may point towards a roughly isotropic fragmentation. All three of the parent remnants are situated proximally to the parents, suggesting they received minimal perturbations following the event.

6. VELOCITY PERTURBATIONS

The velocity perturbations of fragments are calculated in the downrange (along-track), radial, and cross-range (out-of-plane) directions using Equations 6, 7, 8 respectively [22]. Variables with an apostrophe pertain to the fragment.

$$dv_d = \frac{\cos(\varepsilon)}{r}\sqrt{\mu\, a'\,(1-e'^2)} - v_d \tag{6}$$

$$dv_r = \pm\sqrt{\mu\,(\frac{2}{r}-\frac{1}{a'}) - \frac{\mu}{r^2}\,a'\,(1-e'^2)} - |v_r| \tag{7}$$

$$dv_x = \frac{\sin(\varepsilon)}{r}\sqrt{\mu\, a'\,(1-e'^2)} \tag{8}$$

Here, μ refers to the gravitational parameter, a is the semi-major axis, e is the eccentricity, and r is the geocentric distance. v_d and v_r refer to the downrange and cross-range velocities of the parent object (defined in Equations 9 and 10). The plane-change angle, ε, is defined in Equation 11 – i is the inclination of the object, while λ refers to the latitude of fragmentation.

$$v_d = \frac{\sqrt{\mu}}{r}\sqrt{a\,(1-e^2)} \tag{9}$$

$$v_r = \pm\frac{\sqrt{\mu}}{r}\sqrt{a\,e^2 - \frac{(r-a)^2}{a}} \tag{10}$$

$$\varepsilon = \pm\cos^{-1}\left(\frac{\cos(i)\cos(i') + \sqrt{\cos^2(\lambda)-\cos^2(i)}\sqrt{\cos^2(\lambda)-\cos^2(i')}}{\cos^2(\lambda)}\right) \tag{11}$$

The signs of dv_r and v_r are positive when the object is ascending and negative when it is descending.

The total velocity, dv, for a fragment is calculated using Equation 12.

$$dv = \sqrt{dv_d^2 + dv_r^2 + dv_x^2} \tag{12}$$

Due to the nature of these equations, some fragments may have indeterminate radial velocities when their eccentricities are too small (complex values arise from the square root). The plane-change angle, ε, is complex when the latitude of fragmentation exceeds the inclination, resulting in indeterminate downrange and cross-range velocities. This was the case with Event 3, with a significant number of fragments resulting in indeterminate downrange and cross-range velocities at the breakup time of 18:57, 6th April 2019. By slightly changing the breakup time on the same date (19:12 for Vimpel fragments, 19:28 for Spacetrack fragments, and 20:21 for AIUB fragments), the fragment velocities were determinable. While specific values of the velocity and angular perturbations change for different breakup times, broader trends remain the same and are still useful for the purpose of this investigation.

6.1. Event 1 (2009-047B)

Fragment Velocity Frequencies:

Figure 4 shows the velocity perturbations on the fragments and their relative frequencies for Event 1. Most of the fragments have very low velocity perturbations in the downrange and cross-range directions, the former mostly ranging 0-50 m/s (backward for AIUB and forwards for Vimpel) and the latter, 0-25 m/s (mostly downwards). While the Vimpel fragments follow the same cross-range trend as the AIUB fragments, they seem to be moving in opposite directions in both the downrange and radial components. Interestingly, the AIUB fragments appear to have a wide range of radial velocities (in comparison to the other two components), with the majority of the fragments being perturbed radially outwards, unlike the radially inward perturbations of the Vimpel fragments. The three outliers, mentioned in section 5.1, have the following significant downrange and cross-range velocities respectively: 1. 906 m/s, -170 m/s, 2. 1031 m/s, 306 m/s, 3. 1095 m/s, -129 m/s.

The radial velocities for these fragments are indeterminate due to their near-zero eccentricities. Figure 5 is interesting as it departs from the typically exponential trend of fragment velocities that has been seen in prior events (such as the NOAA-3 and Landsat-1 Delta second stage fragmentations). Instead of the highest number of fragments possessing velocities in the lowest range, more of the AIUB fragments have slightly larger velocities, totalling 50-100 m/s. All of the Vimpel fragments are contained in the 0-50 m/s range.

2D and 3D Fragment Velocity Distributions:

Figure 6 shows the velocity distributions in the 2D plane. It is immediately evident that both the AIUB and Vimpel parent remnants encountered very small perturbations, both lying close to the origin. The 'line' patterns formed by the AIUB fragments suggests that fragments with higher radial velocities tend to have higher downrange velocities for this event. While the dvx-dvd plot is fairly isotropic in nature, the plots indicate a high number of AIUB fragments possess large positive radial velocities. The 3D plot in Figure 7 reiterates these observations and emphasizes the radially outward perturbation on the AIUB fragments. Conversely, the Vimpel fragments are mostly perturbed radially inwards. The parent remnants are obscured by the other fragments in the 3D plot but are located close to the origin.

6.2. Event 2 (2014-055B)

Fragment Velocity Frequencies:

Figure 8 shows the velocity perturbations on the fragments and their relative frequencies for Event 2. It must be noted that 31 fragments of Spacetrack produced indeterminate dvd and dvx values, which were thus replaced with 0, likely skewing the Spacetrack distributions. AIUB, Vimpel, and Spacetrack fragments appear to be mostly in agreement in the velocity ranges for the downrange and radial components. AIUB data indicates more fragments sped up along the orbit while the Vimpel data indicates otherwise, with the same speed range of 0-50 m/s. All three data point towards more fragments with radially outward behaviour with speeds of 0-50 m/s. The cross-range velocities are rather interesting, with Vimpel fragments showing an almost equal upward and downward perturbation. Slightly more Vimpel fragments possess speeds ranging 0-25 m/s directed upward; Most of the Spacetrack fragments also lie in this low-velocity range. AIUB fragments appear to have received a significantly stronger perturbation upwards, with most of the velocities in the 75-125 m/s range.
The dv plot in Figure 9 shows that both AIUB and Spacetrack fragments depart from an exponential distribution; more AIUB fragments are found in the 100-150 m/s range, while most (measurable) Spacetrack fragments are found in the 50-100 m/s range. The Vimpel fragments followed the more conventional exponential distribution

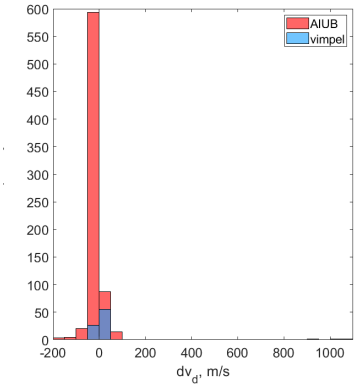

(a) Event 1 (2009-047B): Downrange velocities of fragments.

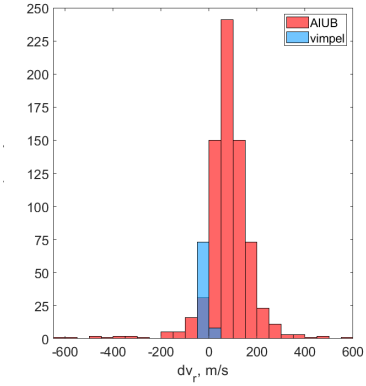

(b) Event 1 (2009-047B): Radial velocities of fragments.

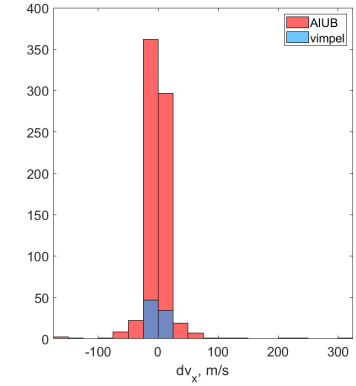

(c) Event 1 (2009-047B): Cross-range velocities of fragments.

Figure 4: Event 1 (2009-047B), Velocity frequencies of fragments.

with a high number of fragments possessing low speeds of 0-50 m/s.

2D and 3D Fragment Velocity Distributions:

Figure 10 shows the velocity distributions in the 2D plane for Event 2. The alignment of the downrange

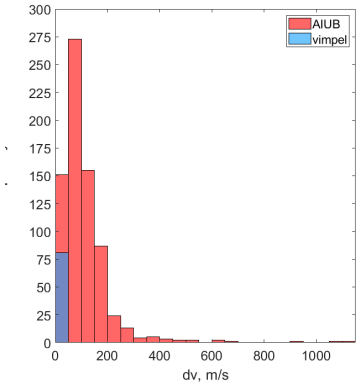

Figure 5: Event 1 (2009-047B), Total velocity perturbations of fragments.

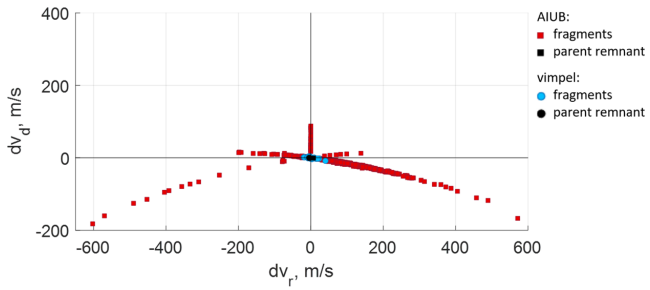

(a) Event 1 (2009-047B): 2D plot of downrange vs. radial velocities of fragments.

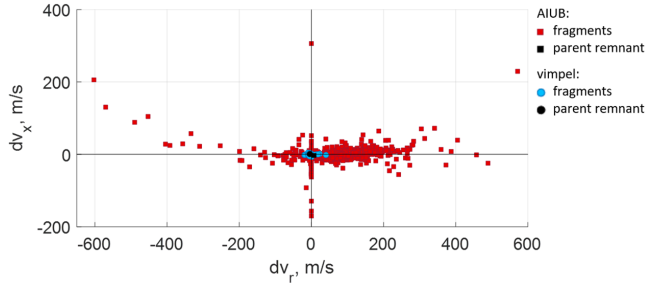

(b) Event 1 (2009-047B): 2D plot of cross-range vs. radial velocities of fragments

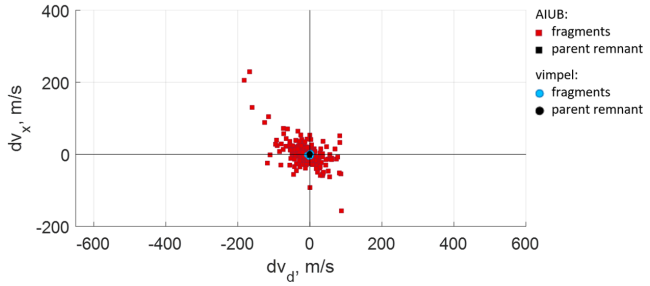

(c) Event 1 (2009-047B): 2D plot of cross-range vs. downrange velocities of fragments

Figure 6: Event 1 (2009-047B), 2D velocity distributions of fragments

and radial velocities of the three data is reiterated in the

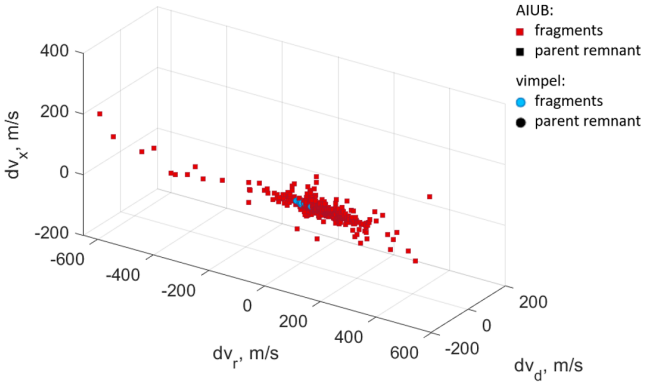

Figure 7: Event 1 (2009-047B), 3D velocity distributions of fragments.

dvd-dvr plot in Figure 10a. The distribution is fairly isotropic and the parent remnants are located in the centre. Similar to Event 1, the parent remnants received very small dvd and dvr perturbations. The AIUB data contains a significant amount of dvx fragments that stray away from the Vimpel and Spacetrack clusters, particularly evident in Figure 10c. Additionally, the AIUB parent remnant appears to have received a large upward perturbation and is situated amid its fragment cluster.

The 3D plot in Figure 11 shows the AIUB and Vimpel fragments as two distinct clusters. The Spacetrack appear to be interspersed between the Vimpel fragments. The AIUB fragments cover a significantly larger range of velocities as inferrable from the visual spread of the data.

6.3. Event 3 (2018-079B)

Fragment Velocity Frequencies:

Figure 12 shows the velocity perturbations on the fragments and their relative frequencies for Event 3. All three data point to roughly isotropic distributions in the downrange and cross-range directions. Both the AIUB and Vimpel fragments indicate a slightly more positive downrange trend; more than half of the fragments sped up along their orbits. Spacetrack data shows the converse trend but is also fairly isotropic. The downrange and radial trends for both the AIUB and Vimpel data are similar, with more fragments possessing positive velocities; conversely, the Spacetrack fragments favour slightly negative velocities. It can be noted that a few AIUB fragments significant radial perturbations both inwards and outwards at velocities around 2 km/s. The cross-range plot is not isotropic in nature for all three data. Both AIUB and Spacetrack point towards a high number of fragments with negative, downward velocities. On the other hand, most of the Vimpel fragments have positive, upward velocities. The range of these cross-range perturbations is notably smaller for the AIUB fragments. Most fragments are contained in the

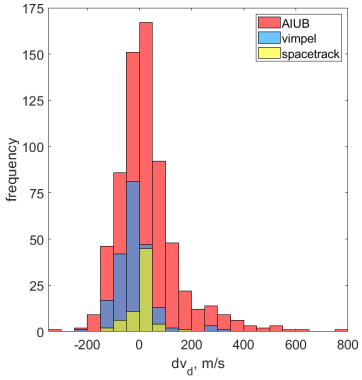

(a) Event 2 (2014-055B): Downrange velocities of fragments.

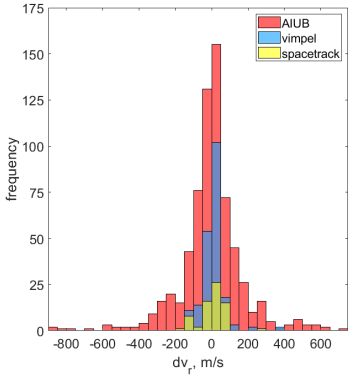

(b) Event 2 (2014-055B): Radial velocities of fragments.

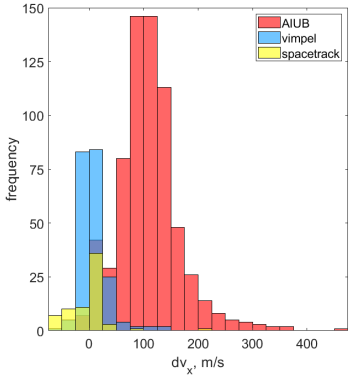

(c) Event 2 (2014-055B): Cross-range velocities of fragments.

Figure 8: Event 2 (2014-055B): Velocity frequencies of fragments.

0-50 m/s range.
The dv plot shown in Figure 13 is quite interesting when the magnitude of the velocities are considered. Many AIUB fragments have significantly higher velocities compared to Events 1 and 2. Vimpel and Spacetrack fragments follow an exponential distribution with high-velocity fragments being low in number. AIUB fragments slightly depart from this trend, with a high

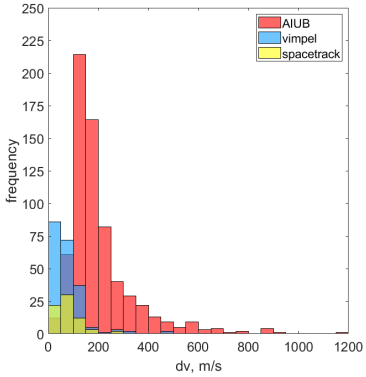

Figure 9: Event 2 (2014-055B), Total velocity perturbations of fragments.

frequency of fragments lying in the 50-100 m/s range; relative to Events 1 and 2, Event 3 is closest to possessing an exponential fragment velocity distribution.

2D and 3D Fragment Velocity Distributions:

Figure 14 shows the velocity distributions in the 2D plane. It is immediately evident that both the AIUB and Vimpel parent remnants encountered very small perturbations. Fragments with higher radial velocities also tend to have higher downrange velocities. While the dvx-dvd plot is fairly isotropic in nature, the plots indicate a high number of fragments possess large positive radial velocities. The 3D plot in Figure 15 reiterates these observations and emphasizes the radially outward perturbation on the AIUB fragments. Conversely, the Vimpel fragments are mostly perturbed radially inwards. The parent remnants are obscured by the other fragments in the 3D plot but are located close to the origin.

7. ANGULAR PERTURBATIONS

The angular perturbations of the fragments are calculated to gain insights into the directions in which the fragments dispersed immediately after the breakup. Two angles akin to the latitude (λ) and longitude (ϕ) of the Earth are defined – these are functions of the velocity perturbations on the fragments as seen in Equations 13 and 14 [22].

$$\lambda = \sin^{-1}\left(\frac{dv_r}{dv}\right) \tag{13}$$

$$\phi = \tan^{-1}\left(\frac{dv_x}{dv_d}\right) + n\,\pi \tag{14}$$

Note: n = 0 for positive downrange velocities; n = 1 for negative downrange and positive cross-range velocities; n = -1 for negative downrange and negative cross-range velocities.
These angular coordinates are projected onto a 'Lambert's equidistant cylindrical projection map', with octants corresponding to different sections of a sphere. The

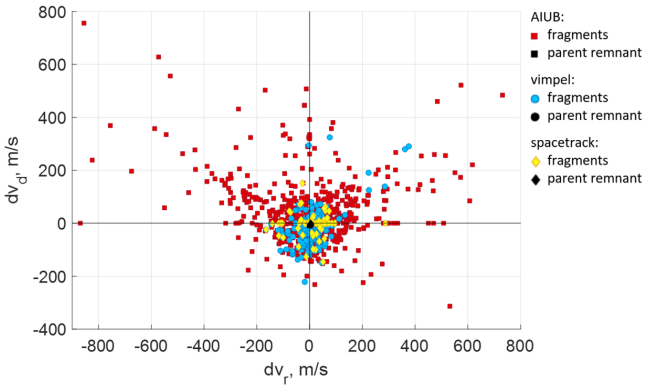

(a) Event 2 (2014-055B): 2D plot of downrange vs. radial velocities of fragments.

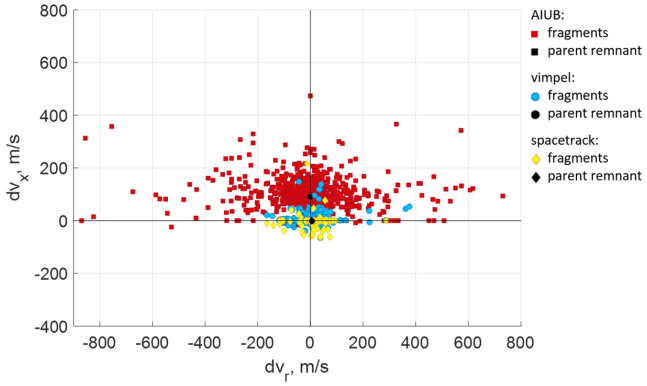

(b) Event 2 (2014-055B): 2D plot of cross-range vs. radial velocities of fragments.

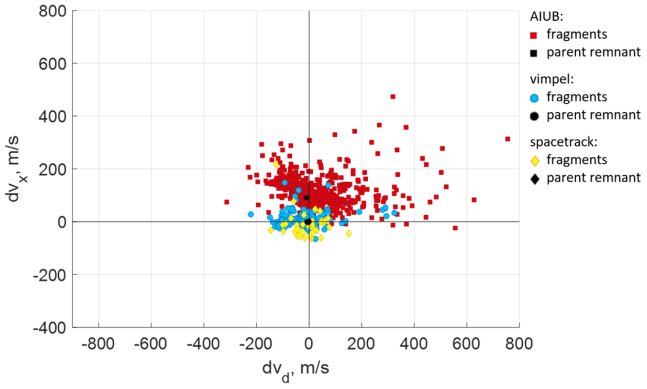

(c) Event 2 (2014-055B): 2D plot of cross-range vs. downrange velocities of fragments.

Figure 10: Event 2 (2014-055B), 2D velocity distributions of fragments.

fragments can be visualized to lie on the surface of this sphere, the centre of which is the fragmentation point.

7.1. Event 1 (2009-047B)

Figure 16 shows the angular distributions of the fragments. There appears to be a clear 'arch' pattern dis-

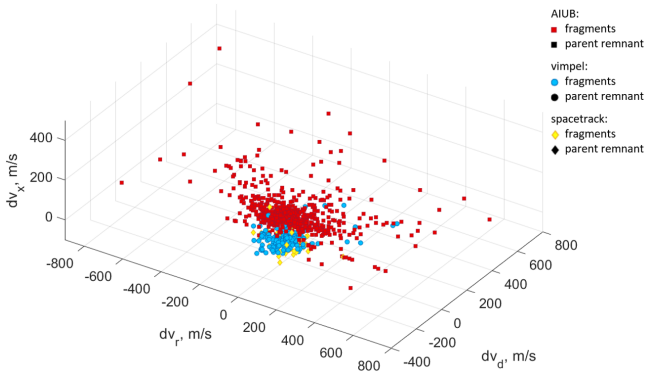

Figure 11: Event 2 (2014-055B), 3D velocity distributions of fragments.

played by both the AIUB and Vimpel fragments. The parent remnants are situated close to the edges of the fragment distributions for both data. The clustering of fragments in this manner is reminiscent of the Clam model [22]. Events characterized by this model have a single rupture point, with most of the fragments emerging on the opposite side of this location. Nearly half the fragments in a Clam event are confined within a fifty-degree cone angle. In the case of Event 1, both data occupy only about a quarter of the surface projection, which is a lot smaller of a section than customary for Clam events, suggesting this may be a variation of one. The rupture location is typically located in the octant diametrically opposite the octant with the most number of fragments. In this case, the 'streak'-like arrangements of the fragments suggest that the rupture point may be in the form of a lengthwise crack as opposed to a circular perforation.

7.2. Event 2 (2014-055B)

Figure 17 shows the angular distributions of the fragments for Event 2. Interestingly, the AIUB and Vimpel distributions are quite incongruous. The AIUB fragments cover roughly two-thirds of the eastern hemisphere of the spherical projection; the parent remnant is roughly in the middle of the cluster. The Vimpel fragments appear to form a vertically oriented torus; the parent remnant is similarly surrounded by other fragments. Not much information can be gleaned from the Spacetrack fragments due to the relatively few 'usable' fragments that had determinable perturbations; these fragments are quite spread out and do not form a noticeable pattern. The Vimpel fragments are in alignment with the Half-Segment model [22]; this is characterized by ruptures at two opposite locations. The two ruptures may exist at low latitudes along the -90 and + 90 longitude regions (about the western and eastern sides of the spherical projection) – this would result in the debris being ejected upwards and downwards to form the ring-like distribution that is observed. On the other hand, the AIUB fragments are evocative of the Clam model, pointing towards the presence of one rupture point. The location of this rupture

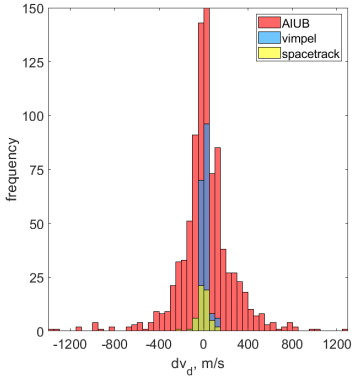

(a) Event 3 (2018-079B): Downrange velocities of fragments.

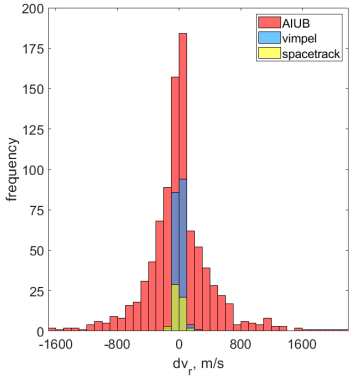

(b) Event 3 (2018-079B): Radial velocities of fragments.

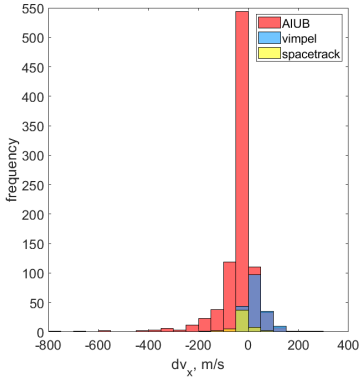

(c) Event 3 (2018-079B): Cross-range velocities of fragments.

Figure 12: Event 3 (2018-079B), Velocity frequencies of fragments.

would face the region diametrically opposite to the fragment cluster, which is largely devoid of fragments.

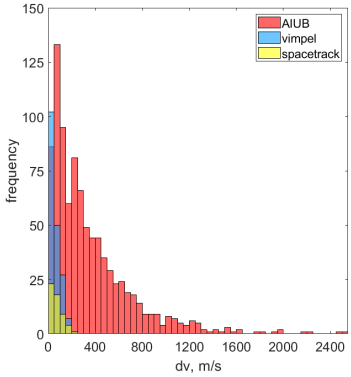

Figure 13: Event 3 (2018-079B), Total velocity perturbations of fragments.

7.3. Event 3 (2018-079B)

The angular distributions of the fragments of Event 3 in 18 show no indication of a singular cluster (Clam model) or the Half-Segment model. The AIUB fragments, for instance, form various clusters indicating the presence of multiple rupture locations. An Octant model (characterized by multiple, roughly equally-spaced rupture locations, with isotropic fragment dispersal [22]) may be applicable here. However, since the fragments are not quite evenly spread, this could be a variation of the Octant model with asymmetric ruptures. It is difficult to discern noticeable patterns from the Vimpel and Spacetrack fragments; however, random dispersal of fragments is also characteristic of the Octant model.

8. INTENSITY OF THE EVENTS

Event intensities are also calculated to gauge the energy expended by the fragmentation event. The intensity is measured using the average total velocity (dv) of the fragments. [22] defines it to be the specific kinetic energy, E, as shown in Equation 15.

$$E = \frac{1}{2}\, dv^2 \tag{15}$$

Higher intensity events are likely to be caused by explosions (leftover propellant combustion, for instance) or collisions, while lower intensity events can be attributed to fragmentations due to drag effects and/or structural failure, or small battery explosions.
The intensities of the three events in m^2/s^2 are shown in Table 4.

The intensities of the three Centaur upper stage events vary substantially based on the data source. This is likely due to the disparity in the number of fragments from each source (this would skew averages), in addition to different propagation times, inevitably leading to accumulating uncertainties. Nevertheless, some patterns can be identified. Fragments stemming from Event 1 possess small

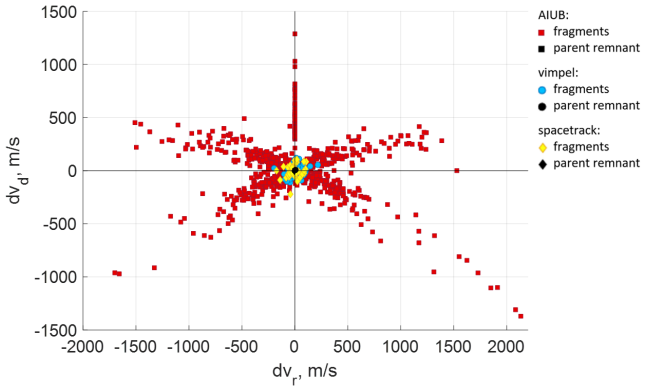

(a) Event 3 (2018-079B): 2D plot of downrange vs. radial velocities of fragments.

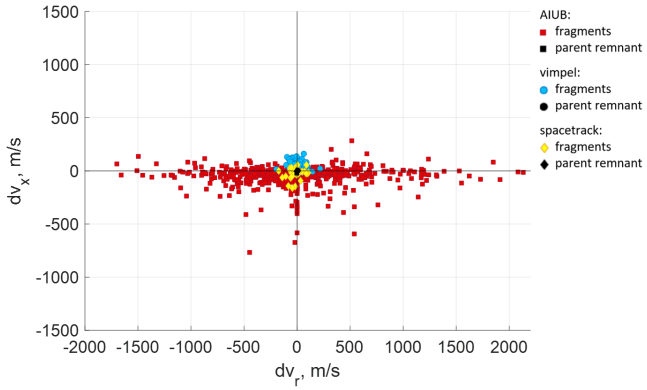

(b) Event 3 (2018-079B): 2D plot of cross-range vs. radial velocities of fragments.

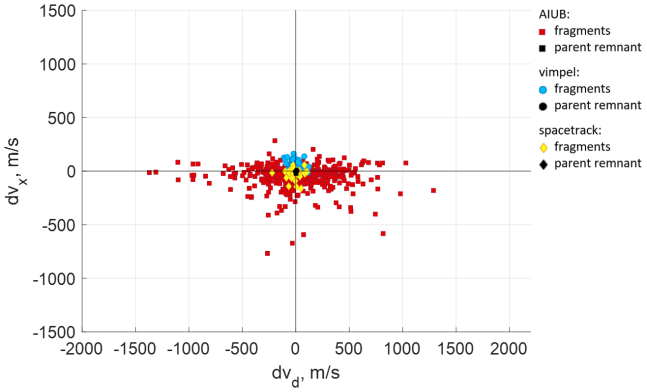

(c) Event 3 (2018-079B): 2D plot of cross-range vs. downrange velocities of fragments.

Figure 14: Event 3 (2018-079B), 2D velocity distributions of fragments.

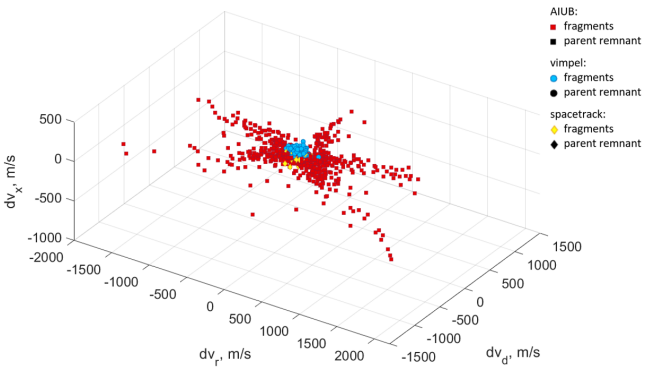

Figure 15: Event 3 (2018-079B), 3D velocity distributions of fragments.

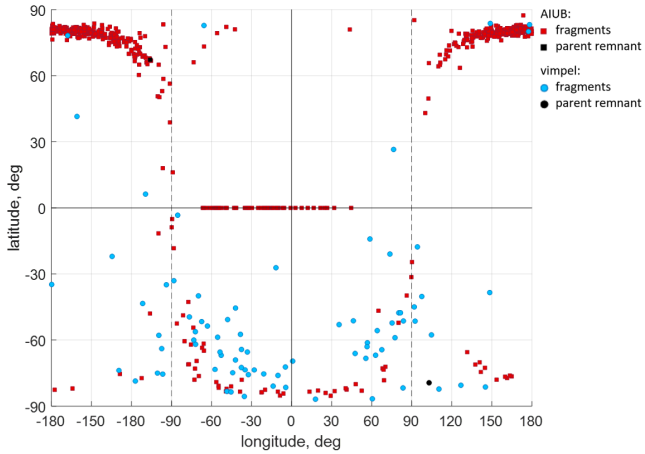

Figure 16: Event 1 (2009-047B), Angular distribution of fragments.

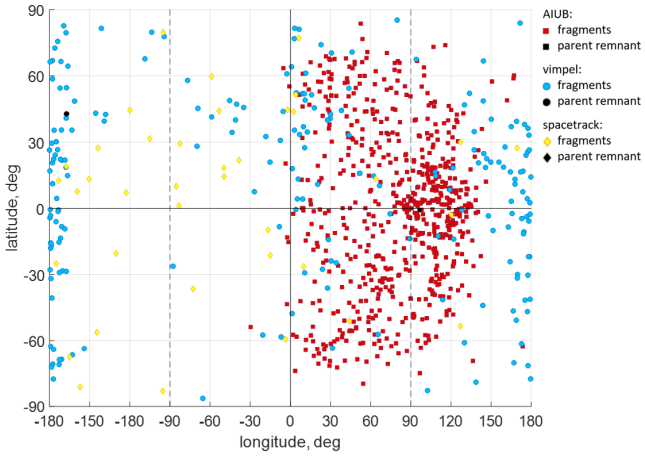

Figure 17: Event 2 (2014-055B), Angular distribution of fragments.

velocities resulting in the lowest intensity of the three events. While both the AIUB and Spacetrack data point towards Event 3 having the highest intensity, the Vimpel data does not. Event 2 appears to have a mid-range intensity, with the average velocities of the Vimpel fragments in relatively close alignment with those of the Spacetrack fragments.

Three fragmentation events pertaining to the Delta upper stages which launched the NOAA-3 (1973-086B), Landsat-1 (1972-058B), and Nimbus-6 (1975-052B) satellites are also included for reference. All three of these events were explosions due to leftover propellant combustion. The high intensity of the Nimbus-6 event is attributable to 245 kg of leftover propellant, compared to

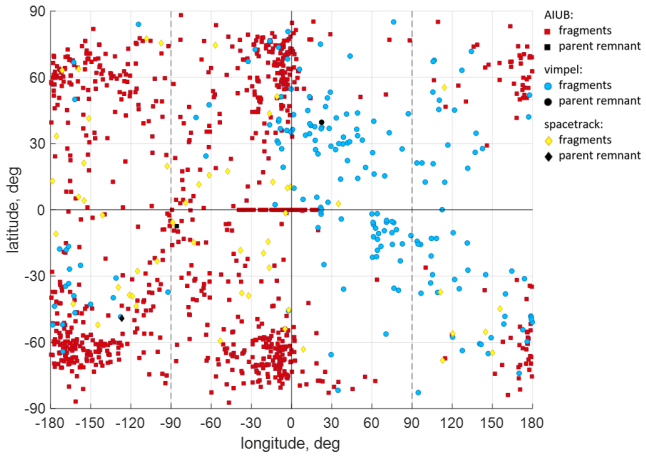

Figure 18: Event 3 (2018-079B), Angular distribution of fragments.

Table 4: Intensities of the Centaur upper stage and select historic events

Event	AIUB	Vimpel	Spacetrack
Event 1 (2009-047B)	5950	19	-
Event 2 (2014-055B)	20673	2836	2555
Event 3 (2018-079B)	55905	1513	8170
NOAA-3	-	-	9613
Landsat-1	-	-	7501
Nimbus-6	-	-	66468
Spot-1	-	-	1511

130-150 kg for the other Delta events [22]. The Spot-1 Ariane event (1986-019C) is believed to have occurred due to a collision with debris and has a noticeably lower intensity.

9. AREA-TO-MASS RATIO

The Area-to-Mass Ratio (AMR) is obtained from the Vimpel catalog and AMR frequencies for the three events are shown in Figure 19.

From the AMR plots, it is evident that most of the fragments for Events 2 and 3 have AMR lower than 0.2 (m^2/kg). Fragments such as these, with low AMR, are typically made of higher density materials such as steel, titanium, or dense aluminium alloys [15]. Most of the fragments of Event 1 possess a slightly higher AMR in the 0.2-0.4 range. This could point towards lower-density materials such as electrical components and aluminium alloys. These outcomes are in alignment with the Centaur's construction – the Centaur upper stage uses stainless steel walled propellant tanks. The pressurization system comprises graphite/epoxy composite materials and

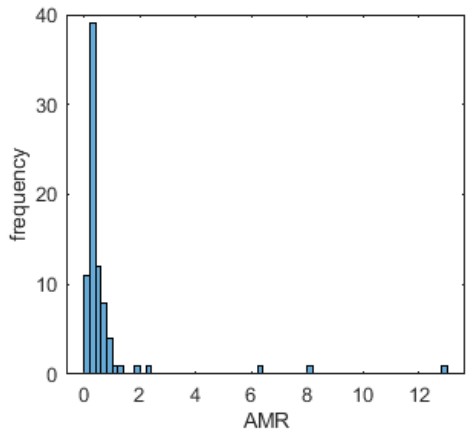

(a) Event 1 (2009-047B), AMR frequencies of fragments.

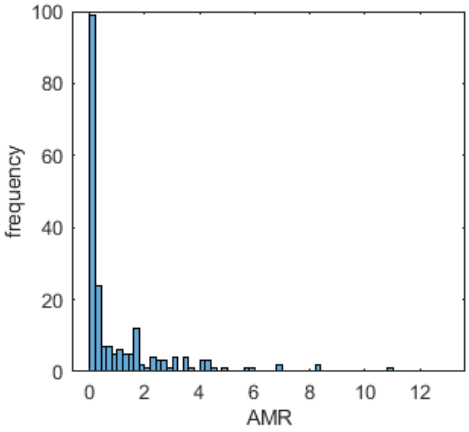

(b) Event 2 (2014-055B), AMR frequencies of fragments.

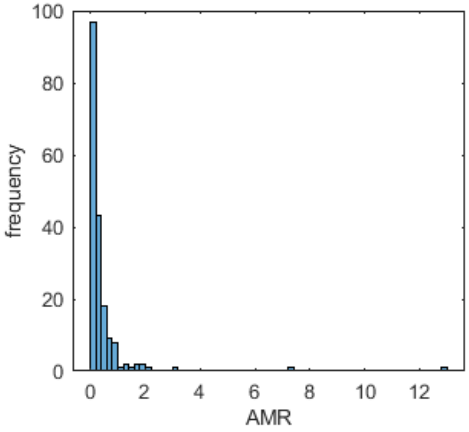

(c) Event 3 (2018-079B), AMR frequencies of fragments.

Figure 19: AMR frequency distributions of the Centaur upper stage events.

aluminium lining materials. The combustion chamber in the RL-10A-4-2 engine is also made of stainless steel

[17]. Event 2 fragments show a larger AMR range, indicating quite a few fragments are made of lower-density materials similar to carbon composites, multi-layer insulation, or solar panel fragments.

10. FRAGMENTATION HYPOTHESES

There is no evidence of another sizeable, catalogued object (such as a satellite or upper stage) having a close encounter with any of the three parent objects at the breakup epoch. Ruling this out and considering the breakup characteristics for each event, some hypotheses can be made regarding their fragmentation causes.

10.1. Event 1 (2009-047B)

The relatively small velocity perturbations of the fragments and the closeness of fragments along the orbit point towards a considerably low-intensity event. As a result, this event is unlikely to be caused by collisions or explosions. The clustered angular distribution of the fragments points to the existence of a single rupture location, possibly a crack. This is likely due to a structural failure of the Centaur body. Material fatigue may have led the upper stage to buckle under stress – such a breakup would result in the small fragment spreading speeds that are observed for this event.

10.2. Event 2 (2014-055B)

Depending on the data source, one can conclude that there are either one (indicated by AIUB data) or two (indicated by Vimpel data) rupture locations. The intensity of the event (based on the Vimpel and Spacetrack fragments) is relatively similar to the Spot-1 event, which is believed to have been caused by a collision with small debris. The AIUB fragments for this event encountered unusually strong cross-range velocity perturbations, which could be indicative of such a collision, resulting in out-of-plane motion. Thus, it is possible that a small piece of debris may have pierced through the Centaur body.

10.3. Event 3 (2018-079B)

The isotropic spread of fragment velocities, high event intensity, and widely dispersed angular patterns of the fragments, all point towards an explosive fragmentation due to leftover propellant combustion. Unlike the Delta upper stage explosions, the fragments in this event spread in various directions but remained in identifiable clusters (as opposed to dispersing haphazardly in all directions). The distinct multidirectionally-dispersed cluster patterns of the AIUB fragments suggest this may be an anomalous propellant tank explosion that is a variation of the Octant model.

11. CONCLUSIONS

To summarize, this investigation of the three Centaur upper stage events shed light on previously unknown information on key breakup characteristics of the fragmentations. Insights into the velocity and angular distributions of the fragments provided crucial information on the immediate aftermath of the events. By discerning trends across the various breakup characteristics, and identifying telltale signs of characteristic explosions or collisions from historic events, cases in support of different hypotheses were steadily built for each event: Event 1, with unusually small fragment velocities and clustered fragments, likely occurred due to a structure failure, giving way to a crack which ultimately fractured the body. On the other hand, Event 2 had a larger intensity and fragment angular distributions which support the possibility of collision with debris, similar to the Spot-1 event. Event 3 had a considerably higher intensity than both Events 1 and 2 – its isotropic fragment distributions indicate the likelihood of an explosion due to leftover propellant.

REFERENCES

1. Agopov V., (2018). *Major fragmentation of Atlas 5 Centaur upper stage 2014-055B (SSN #40209)*, IAA Space Debris Committee meeting, Bremen, Germany, September 29
2. Agopov V., Savin N., (2019). *Updated assessments of the fragmentations of Atlas 5 Centaur upper stages*, IAA Space Debris Committee meeting, Washington D.C., USA, October 19
3. Agopov V., (2019). *Fragmentation of Atlas 5 Centaur upper stage 2009-047B (SSN #35816)*, IAA Space Debris Committee meeting, Paris, France, March 26
4. Badhwar G., Anz-Meador P.D., (1989). *Determination of the Area and Mass Distribution of Orbital Debris Fragments*, Earth, Moon, and Planets, **45**, 29–51
5. Braun V., Lemmens S., Reihs B., Krag H., Horstmann A., (2017). *Analysis of Breakup Events*, 7th European Conference on Space Debris, Darmstadt, Germany, April 18-21
6. Chobotov V.A., Spencer D.B., Schmitt D.L., Gupta R.P., Hopkins R.G., Knapp D.T., (1988). *Dynamics of Debris Motion and the Collision Hazard to Spacecraft Resulting From an Orbital Breakup*, The Aerospace Corporation
7. Cowardin H., Liou J.C., Anz-Meador P., Sorge M., Opiela J., Fitz-Coy N., Huynh T., Krisko P., (2017). *Characterization of Orbital Debris Via Hyper-Velocity Laboratory-Based Tests*, 7th European Conference on Space Debris, Darmstadt, Germany, April 18-21
8. Dimare L., Cicalo S., Rossi A., Alessi E., Valsecchi G., (2019). *In-orbit fragmentation characterization and parent bodies identification by means of orbital distances*, First International Orbital Debris Conference
9. European Space Agency, (2021). *Space debris by the numbers*

10. Flegel S., Bennett J., Lachut M., Moeckel M., Smith C., (2017). *An analysis of the 2016 Hitomi breakup event*, Earth, Planets and Space

11. Healy L., Halpin B., Kindl S., Hoskins B.P., Binz C.R., (2019). *Initial velocity distribution and consequent spatial distribution of fragments*, First International Orbital Debris Conference

12. Hoots F., Sorge M., (2012). *Satellite Breakup Parameter Determination*, The Journal of the Astronautical Sciences, **59**(1&2), 123–143

13. Jehn R., (1990). *Dispersion of Debris Cloud from In-Orbit Fragmentation Events*, 41st Congress of the International Astronautical Federation, Dresden, GDR, October 6-12

14. Kessler D.J., Loftus Jr J.P., (1995). *Orbital Debris as an Energy Management Problem*, Advances in Space Research, **16**(11), 139–144

15. Peterson G., Sorge M., McVey J., (2019). *Forensic Analysis of Debris-Generating Events: Orbcomm FM 16*, First International Orbital Debris Conference

16. Richardson E., Jackson A., Hays M., Bangham M., Blackwood J., Skinner T., Richman B., (2014). *An Experimental Study of Launch Vehicle Propellant Tank Fragmentation*

17. Rudman T., Austad K., (2002). *The Centaur Upper Stage Vehicle*, 4th International Conference on Launcher Technology "Space Launcher Liquid Propulsion", Liege, Belgium, December 3–6

18. Schildknecht T., Vananti A., Cordelli E., (2019). *ESA Optical Surveys to Characterize Recent Fragmentation Events in GEO and HEO*, Advanced Maui Optical and Space Surveillance Technologies Conference (AMOS)

19. Slatton Z., McKissock D., (2017). *Methods of Predicting and Processing Breakups of Space Objects*, 7th European Conference on Space Debris, Darmstadt, Germany, April 18-21

20. Sorge M., Peterson G., McVey J., (2017). *Forensic Analysis of On-Orbit Debris Generation Events*, 7th European Conference on Space Debris, Darmstadt, Germany, April 18-21

21. Tan A., Reynolds R., Schamschula M., (2018). *Gabbard Diagram Formation: The General Theory for Elliptical Orbits*, Advances in Aerospace Science and Applications, **8**(2), 99–112

22. Tan A., Reynolds R.C., (2020). *Theory of Satellite Fragmentation in Orbit*, World Scientific, Singapore